### Highlights

•	Neural	trajectories	in	the	hippocampus	exhib-
	ited gre	ater variabil	ity	durir	ng a working n	nemory
	(WM) t	ask compare	d to	thos	e in the entorhi	nal cor-
	tex and	amygdala re	gio	ns.		

• The distance of neural trajectories between encoding and retrieval states in the hippocampus was memory-load dependent during a WM task.

 Hippocampal neural trajectories fluctuated between the encoding and retrieval states in a taskdependent manner during both baseline and sharpwave ripple (SWR) periods.

• Hippocampal neural trajectories shifted from encoding to retrieval states during SWR period.

# Hippocampal neural fluctuations between memory encoding and retrieval states during a working memory task in humans

Yusuke Watanabe<sup>a,\*</sup>, Yuji Ikegaya<sup>b,c,d</sup>, Takufumi Yanagisawa<sup>a,e</sup>

<sup>a</sup>Institute for Advanced Cocreation studies, Osaka University, 2-2 Yamadaoka, Suita, 565-0871, Osaka, Japan
<sup>b</sup>Graduate School of Pharmaceutical Sciences, The University of Tokyo, 7-3-1 Hongo, Tokyo, 113-0033, Japan
<sup>c</sup>Institute for AI and Beyond, The University of Tokyo, 7-3-1 Hongo, Tokyo, 113-0033, Japan
<sup>d</sup>Center for Information and Neural Networks, National Institute of Information and Communications Technology, 1-4 Yamadaoka, Suita City, 565-0871, Osaka, Japan
<sup>e</sup>Department of Neurosurgery, Osaka University Graduate School of Medicine, 2-2 Yamadaoka, Osaka, 565-0871, Japan

#### **Abstract**

Working memory (WM) plays a pivotal role in multiple cognitive functions, yet the complex neural mechanisms supporting its operation continue to remain unclear. In particular, despite the recognized roles of the hippocampus and sharp-wave ripple complexes (SWRs) – brief, synchronous neural oscillations observed in the hippocampus – in memory consolidation and retrieval, their contribution to WM tasks remains undefined. We demonstrate that during a WM task, multiunit activity patterns in the hippocampus exhibit unique dynamics, particularly during SWR periods. This study analyzed a dataset obtained from intracranial electroencephalogram recordings performed in the medial temporal lobe (MTL) of nine epilepsy patients during an eight-second Sternberg task. We employed Gaussian-process factor analysis to identify low-dimensional neural representations, referred to as 'trajectories,' within the MTL regions during the WM task. The results depicted significant variations in hippocampal neural trajectories as opposed to those in the entorhinal cortex and amygdala. Moreover, the trajectory distance between the encoding and retrieval phases was memory load-dependent. Notably, hippocampal trajectories during the retrieval phase showcased oscillations between encoding and retrieval states, contingent on the task type, particularly displaying a transient shift from encoding to retrieval states during SWRs. These findings emphasize the hippocampus's central role in executing WM tasks and suggest a future research hypothesis: the functional state of the hippocampus transitions from encoding to retrieval during SWRs.

Keywords: working memory, memory load, hippocampus, sharp-wave ripples, humans

7 figures, 3 tables, 221 words for abstract, and 3073 words for main text

#### 1. Introduction

Working memory (WM) significantly influences daily life, and its neural bases continue to be intensively researched. A primary focus of this research is the hippocampus, a structure integral to memory functions [1] [2] [3] [4] [5] [6] [7] [8] [9]. Deepening our understanding of the hippocampus's role in working memory is

critical not only for knowledge advancement but also potentially for cognitive abilities enhancement.

Current evidence suggests a transient, synchronized oscillation known as sharp-wave ripple (SWR) [10] is associated with several cognitive functions. These comprise memory replay [11] [12] [13] [14] [15], memory consolidation [16] [17] [18] [19], memory recall [20] [21] [22], and neural plasticity [23] [24]. These associations posit that SWR could be a core computational feature of hippocampal processing, contributing to working memory performance. However, research on SWR's effects on working memory is relatively sparse [25], being mainly restricted to rodent models engaged in navigation tasks with indefinable memory acquisition and

<sup>\*</sup>Corresponding author. Tel: +81-6-6879-3652 Email: ywata1989@gmail.com

recall timing.

Recent research proposes that low-dimensional representations in hippocampal neurons can elucidate WM task performance. Specifically, the firing patterns of place cells [26] [27] [28] [29] [30] found in the hippocampus, display within a dynamic, nonlinear threedimensional hyperbolic space in rats [31]. Additionally, grid cells in the entorhinal cortex (EC)—a primary route to the hippocampus [32] [33] [34]—showed a toroidal geometry during exploration in rats [35]. These studies, however, are limited by their emphasis on spatial navigation tasks in rodents, which affect the temporal resolution of WM tasks. For instance, the timing of information acquisition by an animal is unclear in these contexts. Therefore, the generalizability of these findings to humans and tasks beyond navigation still requires verification.

Considering these factors, this study explores the hypothesis that hippocampal neurons exhibit unique 'neural trajectories' in low-dimensional spaces, particularly during SWR episodes, when responding to WM tasks. We tested this hypothesis using a high-temporal-resolution dataset of patients performing an eight-second Sternberg task (1 s for fixation, 2 s for encoding, 3 s for maintenance, and 2 s for retrieval). The patients' medial temporal lobe (MTL) intracranial electroencephalography (iEEG) signals were recorded [36]. To analyze low-dimensional neural trajectories, we employed Gaussian-process factor analysis (GPFA), a recognized method for examining neural population dynamics [37].

#### 2. Methods

#### 2.1. Dataset

This study utilized a publicly available dataset that comprises nine epilepsy patients performing a modified Sternberg task [36]. This task includes four phases: fixation (1s), encoding (2s), maintenance (3s), and retrieval (2s). During the encoding phase, participants were presented with a set of four, six, or eight alphabet letters. Their task was to determine whether a probe letter displayed during the retrieval phase was previously presented (the accurate response in a Match IN task) or not (the accurate response for a Mismatch OUT task). Intracranial electroencephalography (iEEG) signals were collected with a 32 kHz sampling rate in the

0.5–5,000 Hz frequency range, using depth electrodes targeting medial temporal lobe (MTL) regions: the anterior head of the left and right hippocampus (AHL and AHR), the posterior body of the hippocampus (PHL and PHR), the entorhinal cortex (ECL and ECR), and the amygdala (AL and AR), as illustrated in Figure 1A and Table 1. The iEEG signals were later downsampled to 2 kHz. Correlations between variables like set size and correct rate were examined (Figure ??S1). Multiunit spike timings were identified using a spike sorting algorithm [38] and the Combinato package (https://github.com/jniediek/combinato)(Figure 1C).

### 2.2. Calculation of neural trajectories using GPFA

Neural trajectories, also known as 'factors', in the hippocampus, EC, and amygdala were calculated using GPFA [37] applied to the multiunit activity data for each session, implemented with the elephant package (https://elephant.readthedocs.io/en/ latest/reference/gpfa.html). The bin size was set to 50 ms, without overlaps. Each factor was znormalized across all sessions, after which the Euclidean distance from the origin (O) was computed. For each trajectory within a region such as AHL, geometric medians (g<sub>F</sub> for fixation, g<sub>E</sub> for encoding, g<sub>M</sub> for maintenance, and g<sub>R</sub> for retrieval phase) were calculated by determining the median coordinates of the trajectory during the four phases. Optimal GPFA dimensionality was established as three using the elbow method obtained by examining the log-likelihood values via a three-fold cross-validation approach (Figure 2B).

### 2.3. Identifying SWR candidates from hippocampal regions

Potential SWR events in the hippocampus were identified using a widely recognized method [39]. LFP signals from a region of interest (ROI), such as AHL, were re-referenced by subtracting the average signal from locations outside the ROI (for instance, AHR, PHL, PHR, ECL, ECR, AL, and AR). The re-referenced LFP signals were then filtered with a ripple-band filter (80–140 Hz) to identify SWR candidates, denoted as SWR<sup>+</sup> candidates. SWR detection was conducted using a published tool (https://github.com/Eden-Kramer-Lab/ripple\_detection) [40], with the bandpass range adjusted to 80–140 Hz for humans [21] [22], contrasting with the initial 150–250 Hz range

typically applied to rodents. Control events for SWR<sup>+</sup> candidates, labeled as SWR<sup>-</sup> candidates, were detected by randomly shuffling the timestamps of SWR<sup>+</sup> candidates across all trials and subjects. The resulting SWR<sup>+</sup>/SWR<sup>-</sup> candidates were subsequently visually inspected.

### 2.4. Defining SWRs from putative hippocampal CA1 regions

Potential SWRs were distinguished from SWR candidates in presumptive CA1 (cornu Ammonis 1) regions. These regions were initially defined as follows: SWR<sup>+</sup>/SWR<sup>-</sup> candidates in the hippocampus were projected into a two-dimensional space based on overlapping spike counts per unit using a supervised approach, UMAP (Uniform Manifold Approximation and Projection) [41]. Clustering validation was conducted by calculating the silhouette score [42] from clustered samples. Regions in the hippocampus, which scored on average above 0.6 across sessions (75th percentile), were identified as putative CA1 areas, resulting in the identification of five electrode positions from five patients. SWR<sup>+</sup>/SWR<sup>-</sup> candidates in these predetermined CA1 areas were classified as SWR+/SWR-, thereby relinquishing their candidate status. The duration and ripple band peak amplitude of SWRs were found to follow log-normal distributions. Each SWR period was segmented relative to the time from the SWR center into pre- (at -800 to -300 ms from the SWR center), mid-(at -250 to +250 ms), and post-SWR (at +300 to +800 to +800ms) times.

### 2.5. Statistical evaluation

Both the Brunner–Munzel test and the Kruskal-Wallis test were administered using the SciPy package in Python [43]. Correlational analysis was performed by determining the rank of the observed correlation coefficient within its associated set-size-shuffled surrogate using a customized Python script. The bootstrap test was performed with an in-house Python script.

### 3. Results

3.1. iEEG recording and neural trajectory in MTL regions during a Sternberg task

Our analysis utilized a publicly accessible dataset [36], comprised of LFP signals (Figure 1A) from MTL

regions (Table 1), recorded during the execution of a modified Sternberg task. From these LFP signals, we extracted SWR+ candidates filtered in the 80-140 Hz ripple band (Figure 1B), originating from all hippocampal regions (refer to the Methods section). Meanwhile, we defined SWR- candidates, control events for SWR<sup>+</sup> candidates, at the same timestamps but distributed across different trials (Figure 1). The dataset also included multiunit spikes (Figure 1C), identified using a spike sorting algorithm [38]. Applying GPFA [37] to 50-ms windows of binned multiunit activity without overlaps, we determined the neural trajectories, or factors, of MTL regions by session and region (Figure 1D). We normalized each factor per session and region, for example, session #2 in AHL of subject #1, then calculated the Euclidean distance from the origin (O) (Figure 1E).

### 3.2. Hippocampal neural trajectory correlation with a Sternberg task

Figure 2A displays the distribution of median neural trajectories, which composed of 50 trials, within the three main factor spaces. Using the elbow method, we determined three as the optimal embedding dimension for the GPFA model (Figure 2B). The trajectory distance from the origin (O) — represented as  $\|g_F\|$ ,  $\|g_E\|$ ,  $\|g_M\|$ , and  $\|g_R\|$  — in the hippocampus exceeded the corresponding distances in the EC and amygdala (Figure 2C & D).

We also calculated the distances between the geometric medians of four phases, namely  $\|g_Fg_E\|$ ,  $\|g_Fg_M\|$ ,  $\|g_Fg_M\|$ ,  $\|g_Eg_M\|$ ,  $\|g_Eg_M\|$ , and  $\|g_Mg_R\|$ . The hippocampus exhibited larger distances between phases compared to the EC and the amygdala.<sup>2</sup>

3.3. Memory-load-dependent neural trajectory distance between encoding and retrieval states in the hippocampus

We observed a negative correlation between the correct rate of trials and the set size, indicating the num-

<sup>&</sup>lt;sup>1</sup>Hippocampus: Distance = 1.11 [1.01], median [IQR], n = 195,681 timepoints; EC: Distance = 0.94 [1.10], median [IQR], n = 133,761 timepoints; Amygdala: Distance = 0.78 [0.88], median [IQR], n = 165,281 timepoints.

<sup>&</sup>lt;sup>2</sup>Hippocampus: Distance = 0.60 [0.70], median [IQR], n = 8,772 combinations; EC: Distance = 0.28 [0.52], median [IQR], n = 5,017 combinations (p < 0.01; Brunner–Munzel test); Amygdala: Distance = 0.24 [0.42], median [IQR], n = 7,466 combinations (p < 0.01; Brunner–Munzel test).

ber of letters to be encoded, during the Sternberg task (Figure 3A).<sup>3</sup> Simultaneously, we found a positive correlation between the response time and set size (Figure 3B).<sup>4</sup>.

Further, we identified a positive correlation between the set size and the trajectory distance separating the encoding and retrieval phases ( $\log_{10}||g_Eg_R||$ ) (Figure 3C).<sup>5</sup>. However, distances between other phase combinations did not show statistically significant correlations (Figures 3D and ??).

### 3.4. Detection of hippocampal SWR from putative CA1 regions

To improve the accuracy of the recording sites and SWR detection, we estimated the electrode placements in the CA1 regions of the hippocampus using distinctive multiunit spike patterns during SWR events. We embedded SWR<sup>+</sup>/SWR<sup>-</sup> candidates from each session and hippocampal region in a two-dimensional space using UMAP (Figure 4A).<sup>6</sup> Using the silhouette score as a clustering quality metric (Figure 4B and Table 2), we identified recording sites that showed an average silhouette score exceeding 0.6 across all sessions as putative CA1 regions.<sup>7</sup> (Tables 2 and 3). From these, we identified five putative CA1 regions, four of which were not identified as seizure onset zones (Table 1).

We labeled SWR<sup>+</sup>/SWR<sup>-</sup> candidates from these putative CA1 regions as SWR<sup>+</sup> and SWR<sup>-</sup>, respectively<sup>8</sup>

(Table 3). Both SWR<sup>+</sup> and SWR<sup>-</sup>, due to their definitions, presented equivalent durations <sup>9</sup>. They followed a log-normal distribution (Figure 4C). An increase in SWR<sup>+</sup> incidence was detected during the initial 400 ms of the retrieval phase<sup>10</sup> (Figure 4D). The peak ripple band amplitude of SWR<sup>+</sup> was higher than that of SWR<sup>-</sup>, following a log-normal distribution (Figure 4E).<sup>11</sup>.

# 3.5. Transient changes in hippocampal neural trajectory during SWR

We examined the 'distance' of the neural trajectory from the origin (O) during SWR events in both encoding and retrieval phases (Figure 5A). Upon observing an increase in distance during SWR, as shown in Figure 5A, we categorized each SWR into three stages: pre-, mid-, and post-SWR. Thus, the distances from O during such SWR intervals are represented as  $\|\text{pre-eSWR}^+\|$ ,  $\|\text{mid-eSWR}^+\|$ , and others.

Consequently,  $\|\text{mid-eSWR}^+\|^{12}$  exceeded  $\|\text{pre-eSWR}^+\|^{13}$ , and  $\|\text{mid-rSWR}^+\|^{14}$  was larger than  $\|\text{pre-rSWR}^+\|$  in both the Match IN and Mismatch OUT tasks.  $^{15}$ .

# 3.6. Visualization of hippocampal neural trajectory during SWR in two-dimensional spaces

Observing 'jumping' of the neural trajectory during SWR (Figure 5), we visualized three-dimensional trajectories of pre-, mid-, and post-SWR events during the encoding and retrieval phases (Figure 6). The distance between these was found to be memory-load dependent (Figure 3).

To provide a two-dimensional visualization, we linearly aligned peri-SWR trajectories by setting g<sub>E</sub> at the

 $<sup>^{3}</sup>$ Correct rate: set size four (0.99 ±0.11, mean ±SD; n = 333 trials) vs. set size six (0.93 ±0.26; n = 278 trials; p < 0.001, Brunner–Munzel test with Bonferroni correction) and set size eight (0.87 ±0.34; n = 275 trials; p < 0.05; Brunner–Munzel test with Bonferroni correction). Generally, p < 0.001 for Kruskal–Wallis test; correlation coefficient = -0.20, p < 0.001.

<sup>&</sup>lt;sup>4</sup>Response time: set size four (1.26  $\pm$ 0.45 s; n=333 trials) vs. set size six (1.53  $\pm$ 0.91 s; n=278 trials) and set size eight (1.66  $\pm$ 0.80 s; n=275 trials). All comparisons p<0.001, Brunner–Munzel test with Bonferroni correction; p<0.001 for Kruskal–Wallis test; correlation coefficient = 0.22, p<0.001

<sup>&</sup>lt;sup>5</sup>Correlation between set size and  $\log_{10}(\|\mathbf{g} \in \mathbf{g}_R\|)$ : correlation coefficient = 0.05, p < 0.001. Specific values:  $\|\mathbf{g} \in \mathbf{g}_R\| = 0.54$  [0.70] for set size four, n = 447;  $\|\mathbf{g} \in \mathbf{g}_R\| = 0.58$  [0.66] for set size six, n = 381;  $\|\mathbf{g} \in \mathbf{g}_R\| = 0.61$  [0.63] for set size eight, n = 395.

<sup>&</sup>lt;sup>6</sup>Consider the AHL in session #1 of subject #1 as an example.

<sup>&</sup>lt;sup>7</sup>The identified regions were the AHL of subject #1, AHR of subject #3, PHL of subject #4, AHL of subject #6, and AHR of subject #9.

<sup>&</sup>lt;sup>8</sup>These definitions resulted in equal counts for both categories:  $SWR^+$  (n = 1,170) and  $SWR^-$  (n = 1,170).

<sup>&</sup>lt;sup>9</sup>These definitions resulted in equal durations for both categories: SWR<sup>+</sup> (93.0 [65.4] ms) and SWR<sup>-</sup> (93.0 [65.4] ms).

 $<sup>^{10}</sup>$ SWR<sup>+</sup> increased against the bootstrap sample; 95th percentile = 0.42 [Hz]; p < 0.05.

 $<sup>^{11}</sup>$ SWR<sup>+</sup> (3.05 [0.85] SD of baseline, median [IQR]; n = 1,170) vs. SWR<sup>-</sup> (2.37 [0.33] SD of baseline, median [IQR]; n = 1,170; p < 0.001: Brunner–Munzel test).

 $<sup>^{12}1.25</sup>$  [1.30], median [IQR], n = 1,281 in Match IN task; 1.12 [1.35], median [IQR], n = 1,163 in Mismatch OUT task

<sup>&</sup>lt;sup>13</sup>1.08 [1.07], median [IQR], n = 1,149 in Match IN task; 0.90 [1.12], median [IQR], n = 1,088 in Mismatch OUT task

 $<sup>^{14}</sup>$ 1.32 [1.24], median [IQR], n = 935 in Match IN task; 1.15 [1.26], median [IQR], n = 891 in Mismatch OUT task

 $<sup>^{15}1.19</sup>$  [0.96], median [IQR], n = 673 in Match IN task; 0.94 [0.88], median [IQR], n = 664 in Mismatch OUT task

origin (0, 0) and  $g_R$  at  $(||g_E g_R||, 0)$ . We then rotated these aligned trajectories around the  $g_E g_R$  axis (the x axis), ensuring the preservation of distances from the origin in original three-dimensional spaces and angles from  $g_E g_R$  in two-dimensional correlates.

In two-dimensional spaces, scatter plot visualization revealed distinct distributions of peri-SWR trajectories based on phases and task types. For instance, the magnitude of ||mid-eSWR<sup>+</sup>|| exceeded ||pre-eSWR<sup>+</sup>|| (Figure 6B), as consistent with our previous findings (Figure 5).

# 3.7. Fluctuations of hippocampal neural trajectories between encoding and retrieval states

Next, we investigated the 'direction' of the trajectory in relation to  $\overline{g_Eg_R}$ , found to be dependent on memory load (Figure 3). We defined the directions of the SWRs by the neural trajectory at -250 ms and +250 ms from their center, labeled as, for example,  $\overline{eSWR}^+$ . We computed the cosine similarities between  $\overline{g_Eg_R}$ ,  $\overline{eSWR}$ , and  $\overline{rSWR}$  during both SWR (SWR<sup>+</sup>)andbaseline periods (SWR<sup>-</sup>) (Figure 7A - D).

 $\overrightarrow{rSWR}^{-} \cdot \overrightarrow{g_Eg_R}$  manifested a biphasic distribution. By computing the difference between the distribution of  $\overrightarrow{rSWR}^{+} \cdot \overrightarrow{g_Eg_R}$  (Figure 7A & B) and that of  $\overrightarrow{rSWR}^{-} \cdot \overrightarrow{g_Eg_R}$  (Figure 7C & D), it was possible to discern the contributions of SWR (Figure 7E & F). This analysis indicated a shift in the direction of  $\overrightarrow{g_Eg_R}$  (Figure 7E & F: *red rectangles*).

Moreover, eSWR<sup>+</sup> · rSWR<sup>+</sup> was less than eSWR<sup>-</sup> · rSWR<sup>-</sup> strictly in the Mismatch OUT task (Figure 7F: *pink circles*). Therefore, eSWR and rSWR pointed in opposite directions exclusively in Mismatch OUT task but didn't do so in Match IN task (Figure 7E: *pink circles*).

### 4. Discussion

This study posits that during a working memory (WM) task in humans, hippocampal neurons form distinct trajectories in low-dimensional spaces, particularly during sharp-wave ripples (SWR) periods. Initially, multiunit spikes in the medial temporal lobe (MTL) regions were projected onto three-dimensional spaces during a Sternberg task, using Gaussian-process factor analysis (GPFA) (Figure 1D–E & Figure 2A). The distances of the trajectories across WM phases (||gFgE||,

 $\|g_F g_M\|$ ,  $\|g_F g_R\|$ ,  $\|g_E g_M\|$ ,  $\|g_E g_R\|$ , and  $\|g_M g_R\|$ ) were significantly larger in the hippocampus than in the entorhinal cortex (EC) and amygdala (Figure 2E), indicating dynamic neural activity in the hippocampus during the WM task. In addition, within the hippocampus, the distance of the trajectory between the encoding and retrieval phases (||g<sub>F</sub>g<sub>E</sub>||) showed a positive correlation with memory load (Figure 3C-D), which reflects WM processing. The hippocampal neural trajectory briefly expanded during SWR events (Figure 5) and alternated between encoding and retrieval states, transitioning from the encoding to the retrieval state during SWR events (Figure 7). These findings provide insights into hippocampal neural activity during a WM task in humans and propose SWRs as crucial to the shift in hippocampal neural states.

The trajectory distance across phases was substantially longer in the hippocampus than in the EC and amygdala, even considering distances from O in these regions (Figure 2C–E). This reinforces the role of the hippocampus in the WM task—consistent with earlier studies showing persistent hippocampal firing during the task's maintenance phase [3] [4] [5] [6]. Applying GPFA to multiunit activity at one-second resolution during the WM task, this study found that the neural trajectory in low-dimensional space exhibited a memory-load dependency between the encoding and retrieval phases, represented as  $\|g_E g_R\|$  (Figure 3). These results support the hippocampus's association with WM processing.

Our analysis targeted putative CA1 regions (Figure 4), a decision supported by several factors. This specific focus stems from existing observations that SWRs synchronize with interneuron and pyramid neuron spike bursts [44] [45] [46] [47], potentially within a 50  $\mu$ m radius of the recording site [48]. Moreover, an elevated incidence of SWRs was identified during the first 0-400 ms of the retrieval phase (Figure 4D), aligning with previous reports of increased SWR occurrence before spontaneous verbal recall [21] [22], which supports our results under a triggered retrieval condition. The observed log-normal distributions of both SWR duration and ripple band peak amplitude (Figure 4C & E) agree with the current consensus in this scientific domain [39]. Therefore, restricting recording sites to putative CA1 regions likely improved the precision, or true positive rate, of SWR detection. However, the trajectory distance increase from O during SWRs (Figure 5) may be artificially inflated towards higher values due to channel selection. This potential bias does not significantly affect our main conclusions.

Interestingly, the trajectory directions oscillated between encoding and retrieval states during both baseline and SWR periods in a task-dependent manner during the retrieval phase (Figure 7C & D). In addition, the balance of this fluctuation transitioned from the encoding to the retrieval state during SWR events (Figure 7E & F). These results align with earlier studies on SWR's role in memory retrieval [21] [22]. Our findings suggest that: (i) neuronal oscillation between encoding and retrieval states occurs during a WM task, and (ii) SWR events indicate the transition from encoding to retrieval states during a WM task.

Furthermore, our study observed WM-task type-specific differences between encoding-SWRs (eSWR) and retrieval-SWRs (rSWR) (Figure 7E–F). Notably, opposing movements of eSWR and rSWR were not observed in the Match IN task but were apparent in the Mismatch OUT task. This observation could be attributed to memory engram theory [49]. The Match IN task presented the participants with previously shown letters, while the Mismatch OUT task introduced a new letter that was not present in the encoding phase. This suggests the essential role of SWR in human cognitive processes.

In conclusion, this study shows that during a WM task in humans, hippocampal activity transitions between encoding and retrieval states, specifically shifting from encoding to retrieval during SWR events. These findings offer novel insights into the neural correlates and functionality of working memory within the hippocampus.

#### References

- [1] W. B. Scoville, B. Milner, LOSS OF RECENT MEMORY AFTER BILATERAL HIPPOCAMPAL LESIONS, Journal of Neurology, Neurosurgery, and Psychiatry 20 (1) (1957) 11-21. URL https://www.ncbi.nlm.nih.gov/pmc/articles/ PMC497229/
- [2] L. R. Squire, The Legacy of Patient H.M. for Neuroscience, Neuron 61 (1) (2009) 6-9. doi:10.1016/j.neuron.2008. 12.023. URL https://www.ncbi.nlm.nih.gov/pmc/articles/ PMC2649674/
- [3] E. Boran, T. Fedele, P. Klaver, P. Hilfiker, L. Stieglitz, T. Grunwald, J. Sarnthein, Persistent hippocampal neural firing and hippocampal-cortical coupling predict verbal working memory

- load, Science Advances 5 (3) (2019) eaav3687. doi:10.1126/sciady.aav3687.
- URL https://www.science.org/doi/10.1126/sciadv.
  aav3687
- [4] J. Kamiński, S. Sullivan, J. M. Chung, I. B. Ross, A. N. Mamelak, U. Rutishauser, Persistently active neurons in human medial frontal and medial temporal lobe support working memory, Nature Neuroscience 20 (4) (2017) 590–601, number: 4 Publisher: Nature Publishing Group. doi:10.1038/nn.4509.
  - URL https://www.nature.com/articles/nn.4509
- [5] S. Kornblith, R. Q. Quiroga, C. Koch, I. Fried, F. Mormann, Persistent Single-Neuron Activity during Working Memory in the Human Medial Temporal Lobe, Current Biology 27 (7) (2017) 1026–1032, publisher: Elsevier. doi:10.1016/j.cub.2017.02.013.
  - URL https://www.cell.com/current-biology/abstract/S0960-9822(17)30149-5
- [6] M. C. M. Faraut, A. A. Carlson, S. Sullivan, O. Tudusciuc, I. Ross, C. M. Reed, J. M. Chung, A. N. Mamelak, U. Rutishauser, Dataset of human medial temporal lobe single neuron activity during declarative memory encoding and recognition, Scientific Data 5 (1) (2018) 180010, number: 1 Publisher: Nature Publishing Group. doi:10.1038/sdata.2018.
  - URL https://www.nature.com/articles/sdata201810
- [7] A. A. Borders, C. Ranganath, A. P. Yonelinas, The hippocampus supports high-precision binding in visual working memory, Hippocampus 32 (3) (2022) 217–230. doi:10.1002/hipo. 23401.
- [8] J. Li, D. Cao, S. Yu, X. Xiao, L. Imbach, L. Stieglitz, J. Sarnthein, T. Jiang, Functional specialization and interaction in the amygdala-hippocampus circuit during working memory processing, Nature Communications 14 (1) (2023) 2921, number: 1 Publisher: Nature Publishing Group. doi:10.1038/s41467-023-38571-w.
  - URL https://www.nature.com/articles/s41467-023-38571-w
- [9] V. Dimakopoulos, P. Mégevand, L. H. Stieglitz, L. Imbach, J. Sarnthein, Information flows from hippocampus to auditory cortex during replay of verbal working memory items, eLife 11 (2022) e78677, publisher: eLife Sciences Publications, Ltd. doi:10.7554/eLife.78677.
  - URL https://doi.org/10.7554/eLife.78677
- [10] G. Buzsáki, Hippocampal sharp wave-ripple: A cognitive biomarker for episodic memory and planning, Hippocampus 25 (10) (2015) 1073–1188, \_eprint: https://onlinelibrary.wiley.com/doi/pdf/10.1002/hipo.22488. doi:https://doi.org/10.1002/hipo.22488. URL https://onlinelibrary.wiley.com/doi/abs/10.1002/hipo.22488
- [11] M. A. Wilson, B. L. McNaughton, Reactivation of hippocampal ensemble memories during sleep, Science (New York, N.Y.) 265 (5172) (1994) 676-679. doi:10.1126/science. 8036517.
- [12] Z. Nádasdy, H. Hirase, A. Czurkó, J. Csicsvari, G. Buzsáki, Replay and Time Compression of Recurring Spike Sequences in the Hippocampus, Journal of Neuroscience 19 (21) (1999) 9497–9507, publisher: Society for Neuroscience Section: ARTICLE. doi:10.1523/JNEUROSCI.19-21-09497.1999.

- URL https://www.jneurosci.org/content/19/21/
  9497
- [13] A. K. Lee, M. A. Wilson, Memory of sequential experience in the hippocampus during slow wave sleep, Neuron 36 (6) (2002) 1183–1194. doi:10.1016/s0896-6273(02)01096-6.
- [14] K. Diba, G. Buzsáki, Forward and reverse hippocampal placecell sequences during ripples, Nature Neuroscience 10 (10) (2007) 1241-1242, number: 10 Publisher: Nature Publishing Group. doi:10.1038/nn1961. URL https://www.nature.com/articles/nn1961
- [15] T. J. Davidson, F. Kloosterman, M. A. Wilson, Hippocampal replay of extended experience, Neuron 63 (4) (2009) 497–507. doi:10.1016/j.neuron.2009.07.027.
- [16] G. Girardeau, K. Benchenane, S. I. Wiener, G. Buzsáki, M. B. Zugaro, Selective suppression of hippocampal ripples impairs spatial memory, Nature Neuroscience 12 (10) (2009) 1222–1223. doi:10.1038/nn.2384.
  URL http://www.nature.com/articles/nn.2384
- [17] V. Ego-Stengel, M. A. Wilson, Disruption of ripple-associated hippocampal activity during rest impairs spatial learning in the rat, Hippocampus 20 (1) (2010) 1–10. doi:10.1002/hipo. 20707
- [18] A. Fernández-Ruiz, A. Oliva, E. Fermino de Oliveira, F. Rocha-Almeida, D. Tingley, G. Buzsáki, Long-duration hippocampal sharp wave ripples improve memory, Science (New York, N.Y.) 364 (6445) (2019) 1082–1086. doi:10.1126/science.aax0758.
  - URL https://www.ncbi.nlm.nih.gov/pmc/articles/
    PMC6693581/
- [19] J. Kim, A. Joshi, L. Frank, K. Ganguly, Cortical-hippocampal coupling during manifold exploration in motor cortex, Nature (2022) 1–8Publisher: Nature Publishing Group. doi:10.1038/s41586-022-05533-z.
  - URL https://www.nature.com/articles/s41586-022-05533-z
- [20] C.-T. Wu, D. Haggerty, C. Kemere, D. Ji, Hippocampal awake replay in fear memory retrieval, Nature Neuroscience 20 (4) (2017) 571–580. doi:10.1038/nn.4507.
- [21] Y. Norman, E. M. Yeagle, S. Khuvis, M. Harel, A. D. Mehta, R. Malach, Hippocampal sharp-wave ripples linked to visual episodic recollection in humans, Science 365 (6454) (2019) eaax1030. doi:10.1126/science.aax1030.
  - URL https://www.sciencemag.org/lookup/doi/10.
    1126/science.aax1030
- [22] Y. Norman, O. Raccah, S. Liu, J. Parvizi, R. Malach, Hip-pocampal ripples and their coordinated dialogue with the default mode network during recent and remote recollection, Neuron 109 (17) (2021) 2767–2780.e5, publisher: Elsevier. doi:10.1016/j.neuron.2021.06.020.
  - URL https://www.cell.com/neuron/abstract/ S0896-6273(21)00461-X
- [23] C. J. Behrens, L. P. van den Boom, L. de Hoz, A. Friedman, U. Heinemann, Induction of sharp wave-ripple complexes in vitro and reorganization of hippocampal networks, Nature Neuroscience 8 (11) (2005) 1560-1567, number: 11 Publisher: Nature Publishing Group. doi:10.1038/nn1571. URL https://www.nature.com/articles/nn1571
- [24] H. Norimoto, K. Makino, M. Gao, Y. Shikano, K. Okamoto, T. Ishikawa, T. Sasaki, H. Hioki, S. Fujisawa, Y. Ikegaya, Hip-

- pocampal ripples down-regulate synapses, Science (New York, N.Y.) 359 (6383) (2018) 1524-1527. doi:10.1126/science.aao0702.
- [25] S. P. Jadhav, C. Kemere, P. W. German, L. M. Frank, Awake Hippocampal Sharp-Wave Ripples Support Spatial Memory, Science 336 (6087) (2012) 1454–1458, publisher: American Association for the Advancement of Science. doi:10.1126/science.1217230.
  - URL https://www.science.org/doi/abs/10.1126/ science.1217230
- [26] J. O'Keefe, J. Dostrovsky, The hippocampus as a spatial map: Preliminary evidence from unit activity in the freely-moving rat, Brain Research 34 (1971) 171–175, place: Netherlands Publisher: Elsevier Science. doi:10.1016/0006-8993(71) 90358-1
- [27] J. O'Keefe, Place units in the hippocampus of the freely moving rat, Experimental Neurology 51 (1) (1976) 78-109. doi:10.1016/0014-4886(76)90055-8. URL https://www.sciencedirect.com/science/ article/pii/0014488676900558
- [28] A. D. Ekstrom, M. J. Kahana, J. B. Caplan, T. A. Fields, E. A. Isham, E. L. Newman, I. Fried, Cellular networks underlying human spatial navigation, Nature 425 (6954) (2003) 184–188, number: 6954 Publisher: Nature Publishing Group. doi:10.1038/nature01964.
  - URL https://www.nature.com/articles/nature01964
- [29] K. B. Kjelstrup, T. Solstad, V. H. Brun, T. Hafting, S. Leutgeb, M. P. Witter, E. I. Moser, M.-B. Moser, Finite Scale of Spatial Representation in the Hippocampus, Science 321 (5885) (2008) 140–143, publisher: American Association for the Advancement of Science. doi:10.1126/science.1157086.
  - URL https://www.science.org/doi/abs/10.1126/science.1157086
- [30] C. D. Harvey, F. Collman, D. A. Dombeck, D. W. Tank, Intracellular dynamics of hippocampal place cells during virtual navigation, Nature 461 (7266) (2009) 941–946, number: 7266 Publisher: Nature Publishing Group. doi:10.1038/nature08499.
  - URL https://www.nature.com/articles/nature08499
- [31] H. Zhang, P. D. Rich, A. K. Lee, T. O. Sharpee, Hippocampal spatial representations exhibit a hyperbolic geometry that expands with experience, Nature Neuroscience (Dec. 2022). doi:10.1038/s41593-022-01212-4.
  - URL https://www.nature.com/articles/s41593-022-01212-4
- [32] P. A. Naber, F. H. Lopes da Silva, M. P. Witter, Reciprocal connections between the entorhinal cortex and hippocampal fields CA1 and the subiculum are in register with the projections from CA1 to the subiculum, Hippocampus 11 (2) (2001) 99–104, \_eprint: https://onlinelibrary.wiley.com/doi/pdf/10.1002/hipo.1028. doi:10.1002/hipo.1028.
  - URL https://onlinelibrary.wiley.com/doi/abs/10.
    1002/hipo.1028
- [33] N. M. van Strien, N. L. M. Cappaert, M. P. Witter, The anatomy of memory: an interactive overview of the parahippocampal-hippocampal network, Nature Reviews Neuroscience 10 (4) (2009) 272–282, number: 4 Publisher: Nature Publishing Group. doi:10.1038/nrn2614.

- URL https://www.nature.com/articles/nrn2614
- [34] B. A. Strange, M. P. Witter, E. S. Lein, E. I. Moser, Functional organization of the hippocampal longitudinal axis, Nature Reviews Neuroscience 15 (10) (2014) 655–669, number: 10 Publisher: Nature Publishing Group. doi:10.1038/nrn3785. URL https://www.nature.com/articles/nrn3785
- [35] R. J. Gardner, E. Hermansen, M. Pachitariu, Y. Burak, N. A. Baas, B. A. Dunn, M.-B. Moser, E. I. Moser, Toroidal topology of population activity in grid cells, Nature 602 (7895) (2022) 123–128, number: 7895 Publisher: Nature Publishing Group. doi:10.1038/s41586-021-04268-7.
  - URL https://www.nature.com/articles/s41586-021-04268-7
- [36] E. Boran, T. Fedele, A. Steiner, P. Hilfiker, L. Stieglitz, T. Grunwald, J. Sarnthein, Dataset of human medial temporal lobe neurons, scalp and intracranial EEG during a verbal working memory task, Scientific Data 7 (1) (2020) 30, number: 1 Publisher: Nature Publishing Group. doi:10.1038/s41597-020-0364-3.
  - URL https://www.nature.com/articles/s41597-020-0364-3
- [37] B. M. Yu, J. P. Cunningham, G. Santhanam, S. I. Ryu, K. V. Shenoy, M. Sahani, Gaussian-Process Factor Analysis for Low-Dimensional Single-Trial Analysis of Neural Population Activity, Journal of Neurophysiology 102 (1) (2009) 614–635. doi:10.1152/jn.90941.2008.
  - URL https://www.ncbi.nlm.nih.gov/pmc/articles/
    PMC2712272/
- [38] J. Niediek, J. Boström, C. E. Elger, F. Mormann, Reliable Analysis of Single-Unit Recordings from the Human Brain under Noisy Conditions: Tracking Neurons over Hours, PLOS ONE 11 (12) (2016) e0166598, publisher: Public Library of Science. doi:10.1371/journal.pone.0166598.
  - URL https://journals.plos.org/plosone/article?
    id=10.1371/journal.pone.0166598
- [39] A. A. Liu, S. Henin, S. Abbaspoor, A. Bragin, E. A. Buffalo, J. S. Farrell, D. J. Foster, L. M. Frank, T. Gedankien, J. Gotman, J. A. Guidera, K. L. Hoffman, J. Jacobs, M. J. Kahana, L. Li, Z. Liao, J. J. Lin, A. Losonczy, R. Malach, M. A. van der Meer, K. McClain, B. L. McNaughton, Y. Norman, A. Navas-Olive, L. M. de la Prida, J. W. Rueckemann, J. J. Sakon, I. Skelin, I. Soltesz, B. P. Staresina, S. A. Weiss, M. A. Wilson, K. A. Zaghloul, M. Zugaro, G. Buzsáki, A consensus statement on detection of hippocampal sharp wave ripples and differentiation from other fast oscillations, Nature Communications 13 (1) (2022) 6000, number: 1 Publisher: Nature Publishing Group. doi:10.1038/s41467-022-33536-x.
  - URL https://www.nature.com/articles/s41467-022-33536-x
- [40] K. Kay, M. Sosa, J. E. Chung, M. P. Karlsson, M. C. Larkin, L. M. Frank, A hippocampal network for spatial coding during immobility and sleep, Nature 531 (7593) (2016) 185–190. doi: 10.1038/nature17144.
- [41] L. McInnes, J. Healy, N. Saul, L. Großberger, UMAP: Uniform Manifold Approximation and Projection, Journal of Open Source Software 3 (29) (2018) 861. doi:10.21105/joss.00861. URL https://joss.theoj.org/papers/10.21105/

ioss.00861

- [42] P. J. Rousseeuw, Silhouettes: A graphical aid to the interpretation and validation of cluster analysis, Journal of Computational and Applied Mathematics 20 (1987) 53–65. doi:10.1016/0377-0427(87)90125-7.
  - URL https://www.sciencedirect.com/science/article/pii/0377042787901257
- [43] P. Virtanen, R. Gommers, T. E. Oliphant, M. Haberland, T. Reddy, D. Cournapeau, E. Burovski, P. Peterson, W. Weckesser, J. Bright, S. J. van der Walt, M. Brett, J. Wilson, K. J. Millman, N. Mayorov, A. R. J. Nelson, E. Jones, R. Kern, E. Larson, C. J. Carey, Polat, Y. Feng, E. W. Moore, J. VanderPlas, D. Laxalde, J. Perktold, R. Cimrman, I. Henriksen, E. A. Quintero, C. R. Harris, A. M. Archibald, A. H. Ribeiro, F. Pedregosa, P. van Mulbregt, SciPy 1.0 Contributors, SciPy 1.0: fundamental algorithms for scientific computing in Python, Nature Methods 17 (2020) 261–272, aDS Bibcode: 2020NatMe..17..261V. doi:10.1038/s41592-019-0686-2. URL https://ui.adsabs.harvard.edu/abs/2020NatMe..17..261V
- [44] G. Buzsáki, Two-stage model of memory trace formation: a role for "noisy" brain states, Neuroscience 31 (3) (1989) 551–570. doi:10.1016/0306-4522(89)90423-5.
- [45] M. L. V. Quyen, A. Bragin, R. Staba, B. Crépon, C. L. Wilson, J. Engel, Cell Type-Specific Firing during Ripple Oscillations in the Hippocampal Formation of Humans, Journal of Neuroscience 28 (24) (2008) 6104–6110, publisher: Society for Neuroscience Section: Brief Communications. doi:10.1523/JNEUROSCI.0437-08.2008.
  URL https://www.jneurosci.org/content/28/24/6104
- [46] S. Royer, B. V. Zemelman, A. Losonczy, J. Kim, F. Chance, J. C. Magee, G. Buzsáki, Control of timing, rate and bursts of hippocampal place cells by dendritic and somatic inhibition, Nature Neuroscience 15 (5) (2012) 769–775, number: 5 Publisher: Nature Publishing Group. doi:10.1038/nn.3077.
  - URL https://www.nature.com/articles/nn.3077
- [47] N. Hájos, M. R. Karlócai, B. Németh, I. Ulbert, H. Monyer, G. Szabó, F. Erdélyi, T. F. Freund, A. I. Gulyás, Input-output features of anatomically identified CA3 neurons during hippocampal sharp wave/ripple oscillation in vitro, The Journal of Neuroscience: The Official Journal of the Society for Neuroscience 33 (28) (2013) 11677–11691. doi:10.1523/ JNEUROSCI.5729-12.2013.
- [48] E. W. Schomburg, C. A. Anastassiou, G. Buzsáki, C. Koch, The Spiking Component of Oscillatory Extracellular Potentials in the Rat Hippocampus, The Journal of Neuroscience 32 (34) (2012) 11798–11811. doi:10.1523/JNEUROSCI.0656-12.2012.
  - URL https://www.ncbi.nlm.nih.gov/pmc/articles/
    PMC3459239/
- [49] X. Liu, S. Ramirez, P. T. Pang, C. B. Puryear, A. Govindarajan, K. Deisseroth, S. Tonegawa, Optogenetic stimulation of a hippocampal engram activates fear memory recall, Nature 484 (7394) (2012) 381–385, number: 7394 Publisher: Nature Publishing Group. doi:10.1038/nature11028.
  - URL https://www.nature.com/articles/nature11028

#### **Contributors**

Y.W. and T.Y. conceptualized the study; Y.W. performed the data analysis; Y.W. and T.Y. wrote the original draft; and all authors reviewed the final manuscript.

### Acknowledgments

This research was funded by a grant from the Exploratory Research for Advanced Technology (JPM-JER1801).

#### **Declaration of Interests**

The authors declare that they have no competing interests.

### Data and code availability

The data is available on G-Node (https://doi.gin.g-node.org/10.12751/g-node.d76994/).

The source code is available on GitHub (https://github.com/yanagisawa-lab/hippocampal-neural-fluctuation-during-a-WM-task-in-humans).

### **Inclusion and Diversity Statement**

We support inclusive, diverse, and equitable conduct of research.

### **Declaration of Generative AI in Scientific Writing**

The authors employed ChatGPT, provided by OpenAI, for enhancing the manuscript's English language quality. After incorporating the suggested improvements, the authors meticulously revised the content. Ultimate responsibility for the final content of this publication rests entirely with the authors.

### **Tables**

Subject ID	# of sessions	AHL	AHR	PHL	PHR	ECL	ECR	AL	AR	SOZ
1	4	<b>√</b>	n.a.	<b>√</b>	<b>√</b>	<b>√</b>	n.a.	<b>√</b>	n.a.	AHR & LR
2	7	$\checkmark$	$\checkmark$	$\checkmark$	$\checkmark$	$\checkmark$	$\checkmark$	✓	✓	AHR & PHR
3	3	$\checkmark$	$\checkmark$	$\checkmark$	$\checkmark$	✓	✓	✓	n.a.	AHL & PHL
4	2	$\checkmark$	✓	$\checkmark$	$\checkmark$	$\checkmark$	$\checkmark$	$\checkmark$	$\checkmark$	AHL & AHR & PHL & PHR
5	3	✓	n.a.	n.a.	✓	n.a.	n.a.	$\checkmark$	n.a.	DRR
6	6	$\checkmark$	✓	AHL & PHL & ECL & AL						
7	4	$\checkmark$	$\checkmark$	$\checkmark$	$\checkmark$	✓	✓	✓	✓	AHR & PHR
8	5	$\checkmark$	✓	$\checkmark$	$\checkmark$	$\checkmark$	$\checkmark$	$\checkmark$	$\checkmark$	ECR
9	2	✓	✓	✓	✓	✓	✓	✓	$\checkmark$	ECR & AR

**Table 1 – Electrode Distribution within the Dataset** 

This figure denotes the placements of electrodes and seizure onset zones. Regions marked with √were included in the dataset, while those imprinted with n.a. were absent. The abbreviations used are as follows: AHL, left hippocampal head; AHR, right hippocampal head; PHL, left hippocampal body; PHR, right hippocampal body; ECL, left entorhinal cortex; ECR, right entorhinal cortex; AL, left amygdala; AR, right amygdala; SOZ represents the seizure onset zone.

Subject	AHL	AHR	PHL	PHR	
1	$0.60 \pm 0.14$	n.a.	n.a.	$0.1 \pm 0$	
2	$0.21 \pm 0.16$	$0.17 \pm 0.21$	$0.18 \pm 0.22$	$0.20 \pm 0.15$	
3	$0.40 \pm 0.42$	$0.83 \pm 0.12$	n.a.	n.a.	
4	$0.10 \pm 0.00$	$0.10 \pm 0.00$	$0.90 \pm 0.00$	$0.10 \pm 0.14$	
5	n.a.	n.a.	n.a.	n.a.	
6	$0.63 \pm 0.06$	n.a.	n.a.	$0.27 \pm 0.06$	
7	$0.10 \pm 0.00$	$0.35 \pm 0.35$	$0.37 \pm 0.47$	$0.10 \pm 0.00$	
8	$0.13 \pm 0.10$	n.a.	$0.28 \pm 0.49$	n.a.	
9	n.a.	$0.85 \pm 0.07$	$0.15 \pm 0.07$	n.a.	

Table 2 – Silhouette score of UMAP clustering for SWR $^{+}$  candidates and SWR $^{\cdot}$  candidates

The silhouette scores (mean  $\pm SD$  across sessions per subject) for UMAP clustering of SWR<sup>+</sup> candidates and SWR<sup>-</sup> candidates are based on their respective multiunit spike patterns (Figure 4A). The mean scores were 0.205 and the standard deviation was 0.285, calculated for the interquartile range (IQR; Figure 4B).

Subject ID	# of sessions	# of trials	ROI	# of SWRs	SWR incidence [Hz]
#1	2	100	AHL	274	0.34
#3	2	97	AHR	325	0.42
#4	2	99	PHL	202	0.26
#6	2	100	AHL	297	0.37
#9	2	97	AHR	72	0.09
	Total = 10	Total = 493		Total = 1170	$0.30 \pm 0.13 \text{ (mean } \pm \text{SD)}$

Table 3 – Summary of Detected SWR Events

The table provides statistics of presumptive CA1 regions and SWR events. Only the initial two sessions (sessions 1 and 2) from each subject were included in our analysis to reduce sampling bias.

### Figures



Figure 1 – Local Field Potentials (LFP), Multiunit Activity, and Neural Trajectories in the Hippocampus During a Modified Sternberg Task

**A.** Representative wideband LFP signals for intracranial EEG recording from the left hippocampal head are presented. This recording took place while the subject performed a modified Sternberg working memory task. Task stages included fixation (1 s, gray), encoding (2 s, blue), maintenance (3 s, green), and retrieval (2 s, red). **B.** Displays the associated ripple band LFP traces. Note purple and yellow rectangles, which denote the timings for SWR<sup>+</sup> candidates and SWR<sup>-</sup> candidates, respectively (the latter serving as control events for SWR<sup>+</sup>). **C.** A raster plot illustrates multiunit spikes from the LFP traces. These spikes have been sorted using a spike algorithm [38]. **D.** Shows neural trajectories computed by GPFA[37] based on spike counts per unit with 50-ms bins. The geometric median of each phase is marked by dot circles. **E.** Indicates the distance of the neural trajectory from the origin point O.

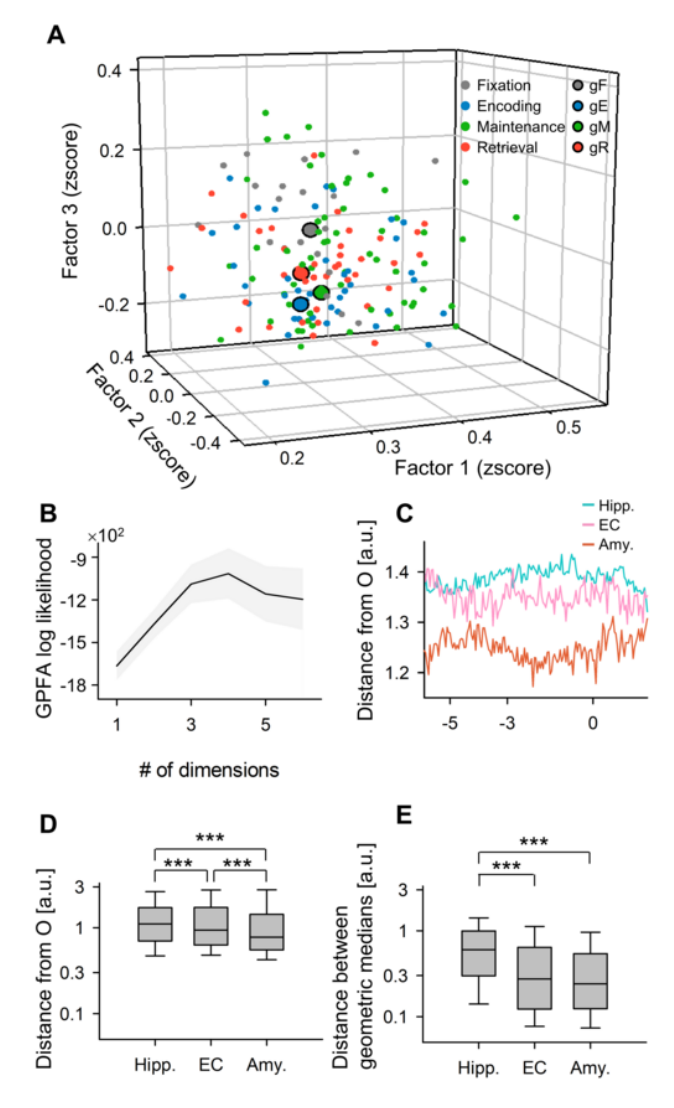


Figure 2 – State-Dependent Trajectories of Hippocampal Neurons

**A.** Neural trajectories are depicted as a point cloud within the first three-dimensional factors derived from GPFA [37]. The smaller dots represent 50-ms neural trajectory bins, and the larger dots with *black* edges denote the geometric medians for each phase in the Sternberg working memory task: fixation ( $\|g_F\|$ , gray), encoding ( $\|g_E\|$ , blue), maintenance ( $\|g_M\|$ , green), and retrieval ( $\|g_R\|$ , red). **B.** The figure presents the log-likelihood of the GPFA models versus the number of dimensions used to embed multiunit spikes found in the medial temporal lobe (MTL) regions. Specifically, the elbow method identified three as the optimal dimension. **C.** This panel displays the distance of the neural trajectories from the origin (O) for the hippocampus (Hipp.), entorhinal cortex (EC), and amygdala (Amy.), plotted against the time elapsed from the probe onset. **D.** The trajectory distance from O within the MTL regions is shown. The hippocampus has the greatest distance, followed by the EC and the Amygdala. **E.** The box plot illustrates inter-phase trajectory distances within the MTL regions.



Figure 3 – Relationship between Trajectory Distance and Memory Load: States of Encoding and Retrieval in the Hippocampus

A. Demonstrates the relationship between set size (number of letters to be encoded) and accuracy in the working memory task (coefficient = -0.20, \*\*\*p < 0.001). **B.** Displays the correlation between set size and response time (coefficient = 0.23, \*\*\*p < 0.001). **C.** Exhibits the influence of set size on the inter-phase distances between the encoding and retrieval phases ( $\|g_Eg_R\|$ ) (correlation coefficient = 0.05, \*\*\*p < 0.001). **D.** Indicates experimental observations of correlations between set size and the following parameters: accuracy, response time,  $\log_{10} \|g_Fg_E\|$ ,  $\log_{10} \|g_Fg_R\|$ ,  $\log_{10} \|g_Fg_R\|$ ,  $\log_{10} \|g_Eg_M\|$ ,  $\log_{10} \|g_Eg_M\|$ ,  $\log_{10} \|g_Eg_M\|$ , and  $\log_{10} \|g_Mg_R\|$  represented by red dots. The gray kernel density plots illustrate the corresponding shuffled surrogate with set size (n = 1,000) (\*\*\*ps < 0.001).

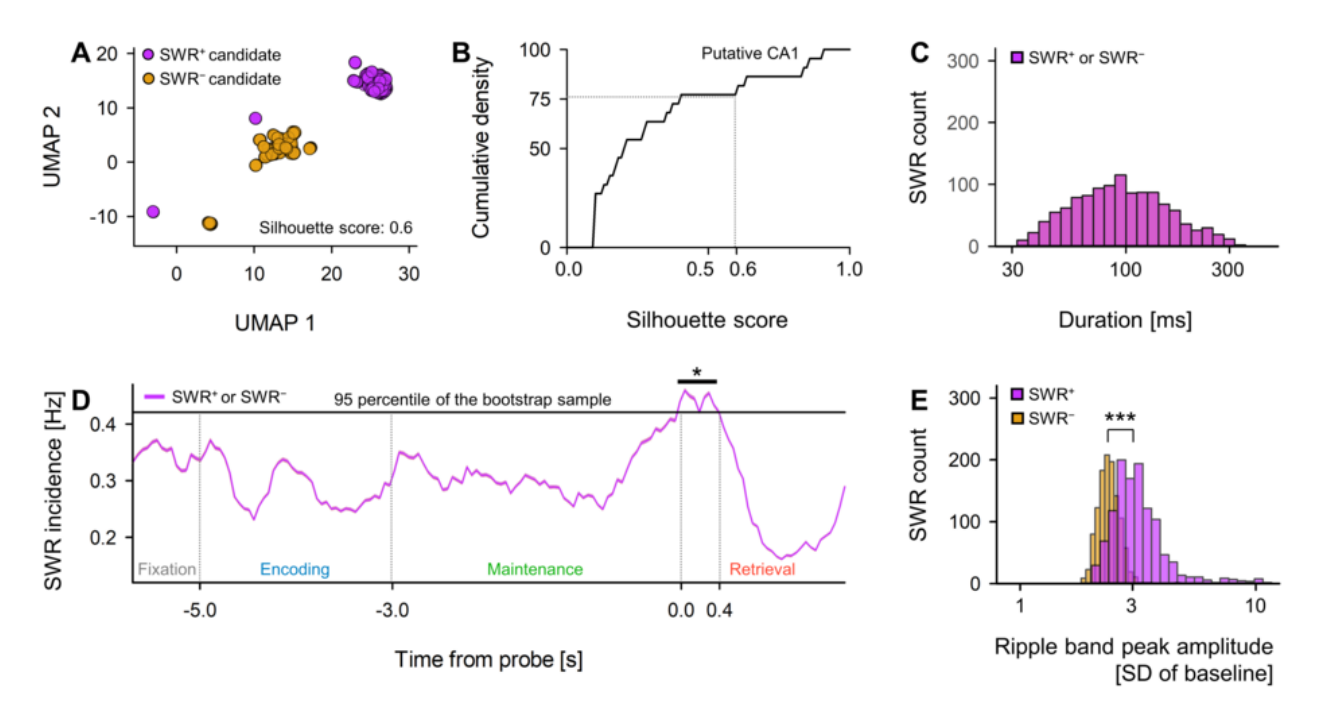


Figure 4 – Detection of SWRs in Putative CA1 Regions

A. Two-dimensional UMAP [41] projection displays multi-unit spikes during SWR<sup>+</sup> candidates (*purple*) and SWR<sup>-</sup> candidates (*yellow*). **B.** A cumulative density plot indicates silhouette scores, reflecting UMAP clustering quality (see Table 2). Hippocampal regions with silhouette scores exceeding 0.60 (equivalent to the 75<sup>th</sup> percentile) are identified as putative CA1 regions. SWR<sup>+</sup> and SWR<sup>-</sup> candidates, which were recorded from these regions, are classified as SWR<sup>+</sup> and SWR<sup>-</sup> respectively (ns = 1,170). **C.** Identical distributions of durations are presented for SWR<sup>+</sup> (*purple*) and SWR<sup>-</sup> (*yellow*), based on their definitions (93.0 [65.4] ms, median [IQR]). **D.** SWR incidence for both SWR<sup>+</sup> (*purple*) and SWR<sup>-</sup> (*yellow*), relative to the probe's timing, is illustrated as a mean  $\pm 95\%$  confidence interval. However, intervals may not be visibly apparent due to their confined ranges, be aware that a significant SWR incidence increase was detected during the initial 400 ms of the retrieval phase (0.421 [Hz], \*p < 0.05, bootstrap test). **E.** Distributions of ripple band peak amplitudes for SWR<sup>-</sup> (*yellow*; 2.37 [0.33] SD of baseline, median [IQR]) and SWR<sup>+</sup> (*purple*; 3.05 [0.85] SD of baseline, median [IQR]) are manifested (\*\*\*p < 0.001, the Brunner–Munzel test).



Figure 5 – Transient Changes in Neural Pathway During SWR Events

A. Presented is the distance from origin (O) of the peri-sharp-wave-ripple pathway (mean  $\pm 95\%$  confidence interval). The intervals may be obscured due to their minimal ranges. **B.** The distance from the origin (O) during the pre-, mid-, and post-SWR periods is demonstrated (\*p < 0.05, \*\*p < 0.01, \*\*\*p < 0.001; Brunner–Munzel test applied). Abbreviations: SWR, sharp-wave ripple events; eSWR, SWR during the encoding phase; rSWR, SWR within the retrieval phase; SWR<sup>+</sup>, positive SWR event; SWR<sup>-</sup>, control events for SWR<sup>+</sup>; pre-, mid-, or post-SWR refer to the time intervals from -800 to -250 ms, from -250 to +250 ms, or from +250 to +800 ms, respectively, all relative to the SWR center.



Figure 6 – Visualization of Neural Trajectories during SWR in Two-Dimensional Spaces

The panels depict hippocampal neural trajectories during SWR projected onto two-dimensional spaces. A. Shows the hippocampal neural trajectories as point clouds during pre-SWR<sup>-</sup> (gray), mid-SWR<sup>-</sup> (yellow), and post-SWR<sup>-</sup> (black). B. Conveys the equivalent for SWR<sup>+</sup> rather than SWR<sup>-</sup>. The projection was executed as follows: First, a linear transformation placed  $g_E$  at the origin O(0,0), and  $g_R$  at ( $||g_Eg_R||, 0$ ). The point cloud was subsequently rotated around the  $g_Eg_R$  axis (similar to the x axis) for adaptation to two-dimensional spaces. Thus, within these two-dimensional spaces, the distances from point O and the angles for the  $g_Eg_R$  axis are retained as in the original three-dimensional spaces created by GPFA. Abbreviations: SWR denotes sharp-wave ripple events; eSWR refers to SWR during the encoding phase; rSWR signals SWR during the retrieval phase; SWR<sup>+</sup>, characterizes an SWR event; SWR<sup>-</sup> signifies control events for SWR<sup>+</sup>; pre-SWR, mid-SWR, or post-SWR, represent the time intervals from -800 to -250 ms, from -250 to +250 ms, or from +250 to +800 ms from the center of the SWR.



Figure 7 – Neural Trajectories Direction during SWRs Based on Encoding and Retrieval States

A–B Shows the kernel density estimation distributions of  $\overrightarrow{eSWR^+} \cdot \overrightarrow{rSWR^+}$  (depicted as pink circles),  $\overrightarrow{eSWR^+} \cdot \overrightarrow{g_Eg_R}$  (blue triangles), and  $\overrightarrow{rSWR^+} \cdot \overrightarrow{g_Eg_R}$  (red rectangles) in the Match In (A) and Mismatch OUT tasks (B). C–D Illustrates the corresponding distributions of  $SWR^-$  instead of those of  $SWR^+$  in A and B. E–F Renders the differences in the distributions of  $SWR^+$  and  $SWR^-$ , detailing the SWR components (E = C - A F = D - B). The biphasic distributions of  $\overrightarrow{rSWR^-} \cdot \overrightarrow{g_Eg_R}$  indicates fluctuations between the encoding and retrieval states during the Sternberg task. Also, contradicting directionality between  $\overrightarrow{eSWR^+}$  and  $\overrightarrow{rSWR^+}$  was observed (pink circles) not in the Match IN task (E), but in Mismatch OUT task (F). Lastly, transition from the retrieval to encoding states are apparent in the SWR components in both Match IN and Mismatch OUT tasks (red rectangles in E–F).